ADVANCED FUNCTIONAL MATERIALS
www.afm-journal.de

Vertical (La,Sr)MnO_3 Nanorods from Track-Etched Polymers Directly Buffering Substrates

By *Adrián Carretero-Genevrier, Jaume Gázquez, Teresa Puig,* Narcís Mestres, Felip Sandiumenge, Xavier Obradors,* and *Etienne Ferain*

A novel and general methodology for preparing vertical, complex-oxide nanostructures from a sol–gel-based polymer-precursor solutions is developed using track-etched polymers directly buffering substrates. This method is able to develop a nanostructure over the entire substrate, the dimensions and localization of the vertical nanostructures being preset by the polymeric nanotemplate. Thereby, nanostructures with lateral sizes in the range of 100 to 300 nm and up to 500 nm in height have been grown. Two examples are presented herein, the latter being the evolution of the initial, metastable nanostructure. Specifically, $La_{0.7}Sr_{0.3}MnO_3$ polycrystalline rods are grown at mild temperatures (800 °C); upon strong thermal activation (1000 °C) they suffer a profound transformation into vertical, single-crystalline $(La,Sr)_xO_y$ nanopyramids sitting on a $La_{0.7}Sr_{0.3}MnO_3$ epitaxial wetting layer. The driving force for this outstanding nanostructural evolution is the minimization of the total energy of the system, which is reached by reducing the grain-boundary, total-surface, and strain-relaxation energies. Finally, advanced electron-microscopy techniques are used to highlight the complex phase separation and structural transformations occurring when the metastable state is overcome.

1. Introduction

The world of nanoscience and nanostructures has explosively emerged in recent years. Many new nanostructures have been realized and new physical properties at the nanoscale have been envisaged. There is still the need for a controlled way of fabrication of nanostructures with high yields, especially when considering functional complex oxides. Additionally, the assembly and organization of vertical nanostructures on substrates is highly demanded for many applications, especially for sensor applications in catalysis, optics and spintronics, and, moreover, the methodologies to generate vertical nanostructures are scare. In this communication, we report on a method to produce arrays of vertical, complex-oxide nanostructures in the form of polycrystalline nanorods and single-crystalline nanopyramids on top of perovskite substrates using chemical solutions to fill nanoporous polycarbonate templates buffering oxide single crystals. The dimensions and localization of these vertical nanostructures are pre-set by the polymeric nanotemplates and nanostructures with lateral sizes in the range of 100 to 300 nm and up to 500 nm in height have been grown.

Chemical methods are able to provide a low cost and high throughput, whereby some approaches have already proved the effective generation of 0D and 1D oxide nanostructures.[1–8] The vapor–liquid–solid process is the most common approach; however, it is restrictive to specific materials.[9,10] Assisted methods to induce self-assembly and self-organization of nanostructures have been extensively demonstrated using top-down nanofabrication methods in semiconductors;[11–16] however, very few works deal with oxide nanostructures[17] and few examples have been reported when these are combined with chemical-solution growth.[18–20] Additionally, special difficulties are encountered when trying to build vertical nanostructures. Track-etched polymer membranes and nanoporous alumina templates have emerged clearly as high-yield approaches for the generation of 1D nanostructures (nanotubes and nanorods).[21–26] While polycrystalline, 1D oxide nanostructures have mostly been reported, especially when chemical-solution methods were used,[22,27,28] only recently have single-crystalline nanowires been generated for the case of polymeric membranes.[7]

2. Results

2.1. Preparation and Structural Properties

Here we present a modified version of using track-etched polymers directly buffering oxide substrates as a novel methodology to generate assisted assemblies of vertical oxide nanostructures using solution methods. Moreover, we have chosen the

[*] Dr. T. Puig, Dr. A. Carretero-Genevrier, Dr. J. Gázquez, Dr. N. Mestres, Dr. F. Sandiumenge, Prof. X. Obradors
Institut de Ciència de Materials de Barcelona (ICMAB)
Consejo Superior de Investigaciones Científicas (CSIC)
08193 Bellaterra, Catalonia (Spain)
E-mail: Teresa.puig@icmab.es
Dr. E. Ferain
Unité de Physique et de Chimie des Hauts Polymères
Université catholique de Louvain
Croix du Sud 1, B-1348 Louvain la Neuve (Belgium)

DOI: 10.1002/adfm.200901971

mixed-valence manganese oxide (manganite) phase due to its interesting functional properties and because the electronic, magnetic, and lattice degrees of freedom can be modified to reach new phenomena at the nanoscale.[24,25,29–34]

We demonstrate that vertical, polycrystalline $La_{0.7}Sr_{0.3}MnO_3$ (LSMO) nanorods with heights of 450–500 nm can be grown on $LaAlO_3$ (LAO) and $SrTiO_3$ (STO) single-crystalline substrates at rather mild temperatures (800 °C) using a sol–gel-based solution–capillarity method. The nanorods stand at the positions previously occupied by the nanopores of the track-etched polymer. Interestingly, these nanorods endure a profound transformation into vertical, single-crystalline, $(La,Sr)_xO_y$ nanopyramids, with heights of 200–250 nm, on an LSMO epitaxial wetting layer upon strong thermal activation (1000 °C). The driving force for this particular nanostructural evolution is the minimization of the total energy of the system by reducing the grain-boundary energy, total-surface, and strain-relaxation energies. Advanced electron-microscopy techniques have highlighted the complex phase separation, as well as the chemical, morphological and structural transformations that occur when the metastable state is overcome. We evidence that the complex-transformation and segregation mechanism suffered by the LSMO polycrystalline nanorods, promoted by thermal activation, occurs provided a good epitaxial match exists between the substrate and the oxide nanostructures.

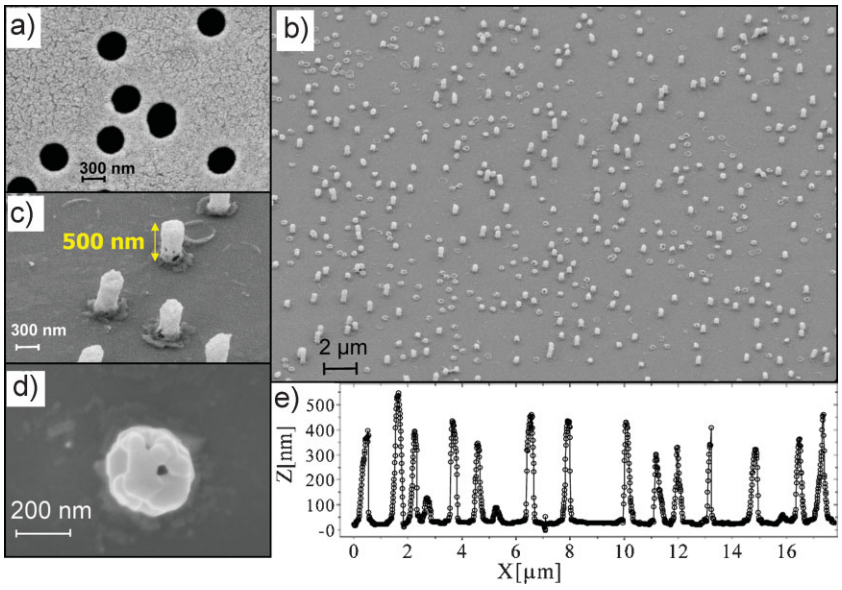

Figure 1. a) SEM image of a track-etched PC polymer template with 350 nm pores and a pore density of 1×10^8 cm^{-2}, deposited on an LAO substrate. b) SEM images of LSMO polycrystalline nanorods vertically grown on the LAO substrate: large area. c) SEM images of LSMO polycrystalline nanorods vertically grown on the LAO substrate: small area. d) Top view of a single nanorod. e) AFM scan indicating the height of the polycrystalline rods.

Along these lines, polycarbonate (PC) films were deposited on $SrTiO_3$ and $LaAlO_3$ (001) substrates by spin coating a PC solution with optimized viscosity and wettability to ensure film adhesion with the substrate. The supported PC films were then irradiated with 220 MeV Ar or 420 MeV Xe ions accelerated using a cyclotron (Cyclotron Research Centre, Louvain-la-Neuve, Belgium and the Grand Accélérateur National Ions de Lourds (GANIL), Caen, France) and a preferential chemical etching was used to produce a random distribution of nanopores.[35,36] The pore diameters were designed to be 100 ± 10, 200 ± 10, 350 ± 20, and 400 ± 20 nm; the pore density was optimized at 1×10^8 cm^{-2} and the irradiated PC film was 1 μm thick. The corresponding characterization was carried out using field-emission scanning electron microscopy (FE-SEM) (see Fig. 1a). The supported nanoporous templates were filled by capillary action using a sol–gel-based polymer-precursor solution of LSMO. After that, the excess of solution was removed by carefully wiping the polymer. The specimens were heated in a furnace at temperatures ranging from 800–1000 °C for 5–10 h in a pure oxygen atmosphere. During this process, the PC polymer (with a decomposition temperature in a single step between 500 and 600 °C) is consequently pyrolyzed, releasing amorphous nanostructures with the preformed shape of the nanopore. Hence, no interference of the template skeleton occurs during the crystallization process of the nanostructures.

Vertical nanostructures, organized accordingly to the polymer template, were obtained by following the above solution-based experimental method where the track-etched polymer buffering single-crystalline substrates were filled with a sol–gel-based polymeric solution. Upon thermal treatment at 800 °C for 5 h, vertical nanorods grew on the STO and LAO (see Fig. 1b,c). For the case of the 400 nm pore size, vertical nanorods with a diameter of 300 nm and a height of 450–500 nm were obtained, where the initial pores were located as observed in the atomic force microscopy (AFM) topographic characterization in Figure 1e. Smaller pore sizes gave rise to nanorods of a smaller diameter in a similar proportion to the one indicated above. X-ray analysis confirmed that the nanorods were LSMO with a rhombohedral structure and the $R\bar{3}c$ space group (Fig. S1, Supporting Information (SI)), and that they were composed of polycrystallites with an average grain size of 65 nm (see Fig. 1d and the Debye–Scherrer analysis of Fig. S1 (SI)). Magnetic characterization (Fig. 2 and Fig. S3 (SI)) demonstrated that the nanorods were ferromagnetic below a Curie temperature of 350 K with a saturation magnetization value close to that of bulk LSMO. The estimated average nanorod volume and pore-density occupancy were determined from the SEM and AFM images.

This is the first time, to our knowledge, that vertical oxide nanorods have been grown, assisted by polymeric track-etched templates using solution-based methods. This method is applicable to other functional materials and especially to other complex oxides. Here we have proved that vertical, LSMO, oxide, polycrystalline nanorods could be obtained in extended areas with good magnetic properties. Remarkably, in this case, a strong nanostructure evolution could be promoted by thermal activation as described below.

Nature certainly tends to minimize the total energy of any system and, under favorable thermal activation, the system will tend to a nanoscale assembly of reduced energy. Here we show that the vertical, polycrystalline, LSMO nanorods have a high interfacial

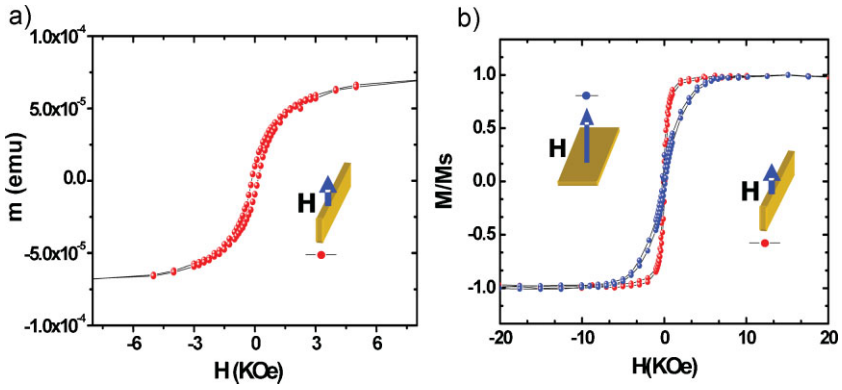

Figure 2. a) Magnetic characterization of the polycrystalline LSMO nanorods where the magnetic moment as a function of magnetic field at 50 K is shown. b) Magnetic characterization of the transformed nanostructures into single-crystalline nanopyramids on an LSMO wetting layer where the in-plane and out-of-plane hysteresis loops at 100 K are displayed.

energy due to their polycrystalline character. Consequently, upon thermal treatment at 1000 °C for 5 h, the vertical polycrystalline nanorods recrystallize into a completely different nanostructure with a lower energy. In other words, we demonstrate that a metastable nanostructure is created with the track-etched-polymer method. Figure 3 reveals that the polycrystalline nanorods disappeared and instead formed faceted nanopyramids with square bases at the same location. Additionally, a wetting layer has expanded underneath the nanopyramid forest covering the single-crystalline substrate. Only a very recent example[37] has shown that nanorods of InAs can emerge from wurtzite InAs pyramids grown on a zinc blende InAs substrate using a specific chemical-beam epitaxial system assisted by Au aerosol particles deposition, though no details were reported on the growth mechanism of the pyramids. As far as we know, the present report is the first time that such a nanostructure transformation has been reported and it clearly demonstrates that completely unexpected phenomena may occur at the nanoscale when diffusion is strongly enhanced. For the case of a 400 nm polymer pore size, vertical nanopyramids with a lateral size of 300 nm and a height of 200–250 nm were formed, as observed in the AFM topographic characterization (Fig. 3d). See Figure S4a (SI) for nanopyramids with a lateral size of 150 nm, obtained from a PC polymer with a 200 nm pore size. It is clear that the nanopyramids grow at the expense of the polycrystalline LSMO nanorods, as exemplified in Figure 3b,c and S4b (SI), where the remaining polycrystalline material is still lying on top of the nanopyramid. However, at the same time, a wetting layer forms underneath the nanopyramids. The surface of this wetting layer is atomically flat with sub-nanometer steps replicating the substrate terraces induced by the substrate miscut angle, which also indicates the very low interfacial energy between the LSMO and LAO. The atomic steps revealed by the AFM image in Figure 3f correspond to two unit cells of the LSMO phase, indicative of a step-bunching growth process.[38] Furthermore, high-resolution transmission electron microscopy (HRTEM) analyses (see Fig. 4a) has identified the wetting layer as being fully strained LSMO with a rhombohedral structure (here indexed by the pseudocubic structure) which grows, cube on cube, on the STO (or LAO) single crystals, (100)[100] LSMO // (100)[100] STO. The thickness of this layer varies depending on the distance from the nearest nanopyramid, ranging from 5 to 20 nm, indicating that the material used to form the wetting layer came from the original polycrystalline nanorods. HRTEM also provides evidence (see Fig. 4b) that the nanopyramids were epitaxially grown on top of this LSMO wetting layer at the sites where the nanorods were previously grown. The nanopyramid facets were found to form an apparent angle of 45° with the LSMO film and an abrupt interface. High-resolution images reveal a characteristic layered atomic structure with a spacing of 0.87 nm, identical to the $(La,Sr)_xO_y$ oxide phase found to outcrop spontaneously from LSMO thin films submitted to extended high-temperature-oxygenation periods,[8] where the outcropping of the $(La,Sr)_xO_y$ islands was accompanied by the formation of $Sr_2Mn_2O_7$ Ruddelsden–Popper inclusions that accounted for the stoichiometric balance. This is a new example

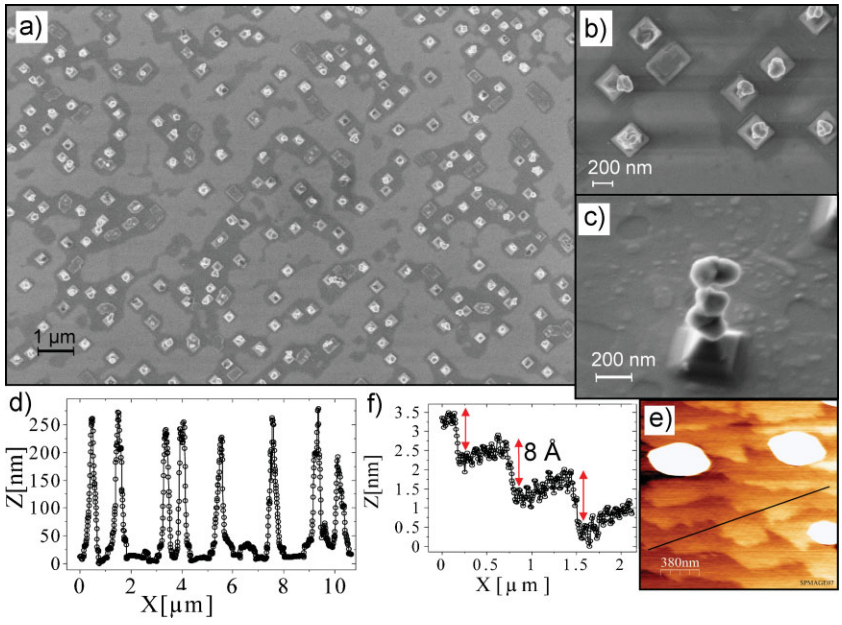

Figure 3. a) SEM image of epitaxial nanopyramids grown on the LAO substrate: large area. b) SEM image of epitaxial nanopyramids grown on the LAO substrate: small area. c) SEM image of epitaxial nanopyramids grown on the LAO substrate: single nanopyramid. d) AFM scan indicating the height of the polycrystalline rods. e) AFM image saturating the nanopyramids to visualize the LSMO wetting layer flatness. f) AFM scan of the LSMO steps following the substrates steps.

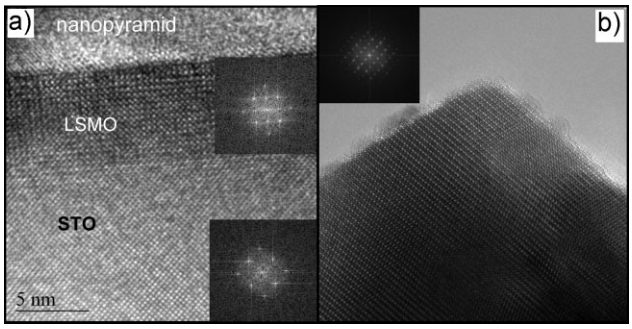

Figure 4. a) HRTEM image of the interface between the STO substrate and the LSMO film and Fourier Transform (FT) of the LSMO wetting layer and STO substrate. b) HRTEM image of an epitaxial nanopyramid and FT of the same image in the [010] zone axis.

of how LSMO epitaxial layers grown by chemical solution (although with completely different solution precursors and growth processes) prefer to segregate $(La,Sr)_xO_y$ oxide nanostructures. It demonstrates the complex chemistry of LSMO layers at high temperatures (1000 °C) where they seems to lose their stability. Energy dispersive X-ray spectroscopy (EDS) analyses performed at different positions of the nanopyramid confirm that the nanopyramids are Mn free (see Fig. 5b,d). Electron energy loss spectroscopy (EELS) analyses (see Fig. S2 (SI)) performed across a nanopyramid/LSMO film interface further confirmed that the Mn L3,2 edge was confined within the LSMO layer (in this case, of 40 nm), whereas the La M5,4 edge persisted across the nanopyramid-film interface. EELS could not give reliable information as to the Sr abundance because of the unfavorable energies associated with its edges.[39] However, since the process transforming the polycrystalline nanorods into nanopyramids and a wetting layer is a kinetically induced process, some pyramids are expected to remain in an intermediate state. This is indeed shown in Figure 5c and 5e, where the TEM image identifies a region with darker contrast within a nanopyramid, which EDS confirmed to be a Mn-rich cluster. Figure 5a shows the EDS analysis at different regions within and beneath the nanopyramids and in the LSMO film in the proximity of a nanopyramid, a distance of approximately 100 nm. From this, we conclude that the Mn/La stoichiometry can strongly vary with values in the range 0 to 1.1, while the stoichiometric ratio for $La_{0.7}Sr_{0.3}MnO_3$ would be 1.4. Hence, this confirms that the $La_{0.7}Sr_{0.3}MnO_3$ polycrystalline nanorods are thermodynamically metastable nanostructures of high energy (large interfacial grain-boundary energy, E_{GB}) that kinetically transform under strong thermal activation into Mn-free, oxide, epitaxial nanopyramids on top of a $La_{1-x}Sr_xMnO_3$ epitaxial wetting layer of variable stoichiometry.

We may now wonder why such a nanostructure has the lowest energy. The fact that the LSMO film wets the substrate completely, growing atomically flat, provides evidence that $\gamma_{s\text{-}LSMO} + \gamma_{LSMO} \leq \gamma_s$, $\gamma_{s\text{-}LSMO}$ being the low interface energy between the substrate and the LSMO crystalline phase, γ_{LSMO} the surface energy of the crystalline phase and γ_s the surface energy of the substrate. It is known that heteroepitaxial growth of (100)[100]LSMO//(100)[100]STO (or LAO), where $E_s(100)$ is the lowest surface energy for cubic perovskites,[40] favors a layer-by-layer growth mode.[41] However, here, a complex transformation of the polycrystalline nanorods into epitaxial nanopyramids on a wetting (100) LSMO layer occurs. This transformation certainly eliminates the interfacial grain-boundary energy, E_{GB}, but also, additionally, should minimize the total energy of the transformed configuration, $E = E_s + E_{relax}$, where E_s and E_{relax} are the total-surface and strain-relaxation energies, respectively. The phase separation that was induced, with $(La,Sr)_xO_y$ nanoislands remaining on top of the LSMO wetting layer, indicates that, at this other interface, $\gamma_{LSMO\text{-}LSO} + \gamma_{LSO} \geq \gamma_{LSMO}$, $\gamma_{LSMO\text{-}LSO}$ being the interfacial energy between the LSMO film and the $(La,Sr)_xO_y$ nanopyramids and γ_{LSO} and γ_{LSMO} being the respective surface energies. This suggests that a strong decrease of the relaxation-strain energy occurs, allowing the increase of surface energy by the nanopyramid free surfaces to be balanced. The final nanostructure can neither be considered to be a consequence of a Stranski–Krastanov growth mode, where coherently strained nanodots are segregated at the surface from a strained wetting layer, driven by the elastic-relaxation term,[42,43] nor a modified Stranski–Krastanov growth involving different heteroepitaxial oxide phases.[8] Instead, the wetting layer builds up simultaneously with the transformation of the polycrystalline nanorods into epitaxial coherent nanopyramids. Hence, it demonstrates that, at the nanoscale, the metastable structures can easily evolve towards the equilibrium state because the involved mass transport is small enough.

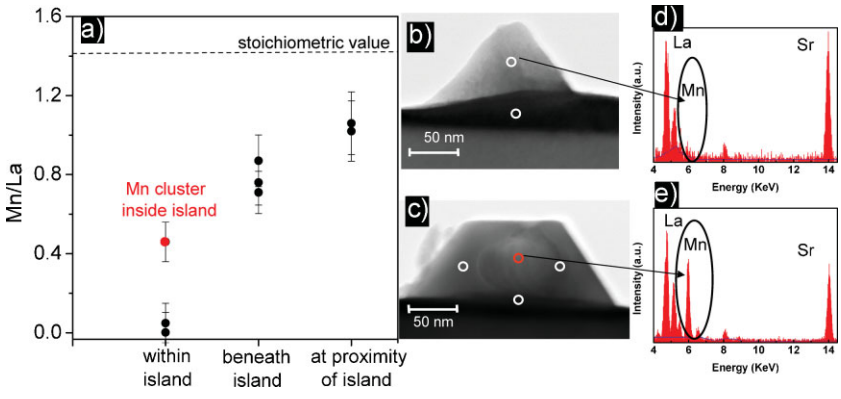

Figure 5. a) Mn/La ratio at different regions of the nanopyramids and the LSMO film. b,c) TEM images of particular nanopyramids: a central region with higher contrast is identified in (c) as being rich in Mn while the rest of the pyramid does not contain Mn, indicating a kinetically driven system. d,e) EDS analysis confirming the results in (b) and (c).

2.2. Magnetic Properties and Applications

Magnetic characterization of these LSMO epitaxial layers with nonmagnetic oxide nanopyramids (see Fig. S3 (SI)) indicates a Curie temperature of 350 K, which is characteristic of the LSMO rhombohedral phase, and a magnetic moment of 5×10^{-5} emu, which, assuming a bulk magnetization of LSMO at 100 K, would imply a layer thickness of 10 nm, which is within the measured range. Additionally, magnetization loops at 100 K under the

in-plane and out-of-plane configurations reveal an in-plane easy-axis magnetization of the epitaxial (100) LSMO film (see Fig. 2). This confirms that the segregated nanopyramids do not apparently modify the macroscopic functional properties of the LSMO film. Therefore, a nanostructured system was achieved, which was composed of an epitaxial LSMO wetting layer with epitaxial vertical nanopyramids grown on top and distributed accordingly to the nanopores of the polymeric template.

This complex nanostructure, although already interesting by itself, has also been tested as a template for the ulterior growth of nanostructured, superconducting $YBa_2Cu_3O_{7-x}$ (YBCO) films using chemical solutions.[44] The LSMO wetting layer offers the interesting advantage of being conductive, chemically compatible with YBCO and having a low lattice mismatch with YBCO ($\varepsilon = +0.78\%$ for (001)[001] YBCO//(100)[100] LSMO). The heteroepitaxies of YBCO/LSMO have been reported previously using physical methods and also recently using an all-solution-based method.[45–47] Details on the heteroepitaxy, structural and physical properties of solution-derived YBCO/LSMO bilayers have been reported elsewhere.[47] Here, we report on the effect of the nanostructured template composed of the nanopyramids and LSMO wetting layer in modifying the pinning of vortices by generating artificial pinning centers and consequent enhancement of the superconducting performances of the nanostructured superconducting film. Figure 6 shows the pinning force as a function of magnetic field at 77 K, as the key magnitude to evaluate vortex pinning of YBCO films grown on top of the mentioned template, in comparison with a standard YBCO film grown on an LAO substrate.[48] Notice that the pinning force, F_p, was increased in the entirety of the magnetic-field range and that the magnetic field at maximum pinning force was shifted to higher magnetic fields for the nanostructured template. In particular, F_p increased by a factor of 2 at 3 T and a factor of 4 at 5 T, at 77 K. Further optimization should be carried out in order to achieve better performance; here, we confirm the potential of these nanostructured templates to improve vortex pinning of superconducting layers.

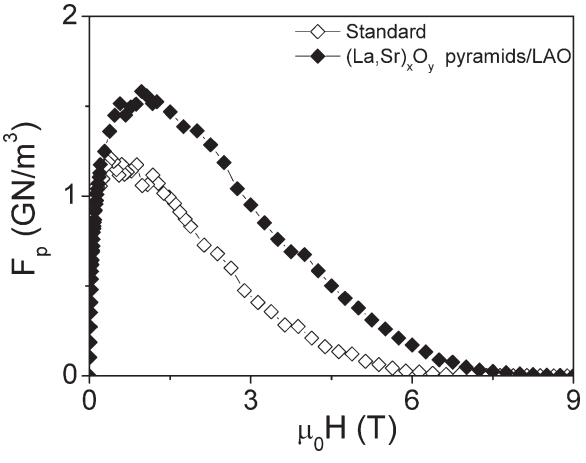

Figure 6. Pinning force as a function of applied magnetic field at 77 K for a YBCO film grown on the nanostructured template composed of $(La,Sr)_xO_y$ nanopyramids and an LSMO wetting layer. The comparison with a YBCO film grown on an LAO substrate is shown.

3. Conclusions

In summary, vertical oxide nanostructures have been grown, assisted by nanoporous polymer templates and their localization is determined by the position of the nanopores. Further ordering in any desired configuration may be attained by arranging the nanopores with the use of extended masks in a cyclotron-radiation facility. This paper has demonstrated that track-etched polymer fabrication, which is nowadays a large-scale industrialized process, can be easily implemented to specific substrates for further growth of low-cost, large-scale, vertical oxide nanostructures by the use of proper solution-based methods. We have presented two types of vertical nanostructures that are produced by using a single sol–gel-based polymeric LSMO precursor solution while varying the thermal annealing. Clearly, the methodology presented here is of general use and opens this field to the growth of other vertical functional oxide nanostructures. In the particular example studied, we have shown evidence that vertical polycrystalline $La_{0.7}Sr_{0.3}MnO_3$ nanorods can be grown on STO or LAO single-crystalline substrates as a thermodynamic metastable phase reached at growth temperatures of 800 °C. The nanorods have the LSMO rhombohedral structure and are ferromagnetic below 350 °C. This nanostructure suffers a complete structural, morphological, and chemical transformation involving a segregation mechanism induced by thermal activation, giving rise to vertical, epitaxial oxide $(La,Sr)_xO_y$ faceted nanopyramids with a square base, segregated on top of a (100) LSMO heteroepitaxial wetting layer. Such an extraordinary transformation at the nanoscale is driven by energy minimization and demonstrates that metastability can be easily overcome when the involved mass transport is small enough. Energy minimization is achieved by reducing the grain-boundary and total-surface energies, as well as the strain-relaxation energy, when transforming the polycrystalline nanorods into a nanopyramids/wetting-layer composite system. The reason for this chemical and structural segregation remains unknown and requires further theoretical analysis. Many applications may be realized using vertical nanostructures; the composite system presented here, formed by a metallic and magnetic LSMO layer with insulating and nonmagnetic oxide nanopyramids, has been used to induce artificial pinning centers in superconducting $YBa_2Cu_3O_7$ films, and the pinning forces have been enhanced at 77 K by factors of 2 and 4 at 3 T and 5 T, respectively.

4. Experimental

Details on the solution preparation have been reported previously [7]. Briefly, high-purity (>99.99%) metal salts, $La(NO_3)_3 \cdot 6H_2O$, $Sr(NO_3)_2 \cdot 4H_2O$, and $Mn(NO_3)_2 \cdot 4H_2O$, were used to prepare aqueous solutions of the corresponding nitrates in their stoichiometric ratios ($La_{0.7}Sr_{0.3}MnO_3$). Ethylene glycol was added with continuous stirring and gradual heating (up to 150 °C) in order to produce a polymerized solution with a concentration of 0.9 M and a viscosity of 30 mPa s. The solution was then basified up to a pH of 3 to avoid reactivity with the polymer. The chemical composition of the final solution was investigated using inductively coupled plasma spectroscopy using a Cambridge Scientific Thermo Elemental Intrepid II XLS spectrometer. The obtained nanostructures were characterized using electron microscopy. A field-emission electron microscope (LEO 1530) was used for the observation of the final nanostructures. High-resolution electron microscopy images were obtained using a Jeol 2011 transmission electron microscope operating

at 200 kV and a Jeol 2010 FEG transmission electron microscope operating at 200 kV, equipped with a Gatan image filter and a 200 kV electron energy-loss spectrometer with an energy resolution of 0.8 eV.

A global X-ray diffraction characterization was carried out using a Bruker AXS GADDS instrument equipped with a 2D X-ray detector. The magnetization measurements were made in a dc superconducting quantum interference device (SQUID) magnetometer (Quantum Design MPMS-XL7) in applied magnetic fields between 0 and 7 T and from 10 to 400 K. The wetting layer and pyramid morphology was investigated using AFM performed in the tapping mode at room temperature using an Agilent 5100 instrument operated in the dynamic mode with a silicon AFM tip. The statistical analysis of the AFM images was carried out using the WSxM software (4.0 SPMAGE07 Edition).

Acknowledgements

We acknowledge the financial support from MICINN (MAT2008-01022, MAT2005-02047, MAT2006-26543-E, NAN2004-09133-CO3-01, Consolider NANOSELECT, FPI and the GICSERV program ''Access to ICTS integrated nano- and microelectronics cleanroom''), Generalitat de Catalunya (Catalan Pla de Recerca SGR-0029 and XaRMAE), CSIC (PIF-CANNAMUS) and the EU (HIPERCHEM, NMP4-CT2005-516858 and NESPA). Serveis Científic-Tècnics from Universitat de Barcelona and Servei de Micròscopia from Universitat Autònoma de Barcelona are acknowledged for their TEM facilities. Supporting Information is available online from WileyInterscience or from the authors.

Received: October 20, 2009
Published online:

[1] I. Szafraniak, C. Harnagea, R. Scholz, S. Bhattacharyya, D. Hesse, M. Alexe, *Appl. Phys. Lett.* **2003**, *83*, 2211.
[2] P. A. Langjahr, T. Wagner, M. Ruhle, F. F. Lange, *J. Mater. Res.* **1999**, *14*, 2945.
[3] R. Bachelet, S. Cottrino, G. Nahelou, V. Coudert, A. Boulle, B. Soulestin, F. Rossignol, R. Guinebretiere, A. Dauger, *Nanotechnology* **2008**, *18*, 9.
[4] A. Roelofs, I. Schneller, K. Szot, R. Waser, *Appl. Phys. Lett.* **2002**, *81*, 5231.
[5] S. Clemens, T. Schneller, A. van der Hart, F. Peter, R. Waser, *Adv. Mater.* **2005**, *17*, 1357.
[6] M. Gibert, T. Puig, X. Obradors, A. Benedetti, F. Sandiumenge, R. Hühne, *Adv. Mater.* **2007**, *19*, 3937.
[7] A. Carretero-Genevrier, N. Mestres, T. Puig, A. Hassini, J. Oro, A. Pomar, F. Sandiumenge, X. Obradors, E. Ferain, *Adv. Mater.* **2008**, *20*, 3672.
[8] C. Moreno, P. Abellán, A. Hassini, A. Ruyter, A. P. d. Pino, F. Sandiumenge, M. Casanove, J. Santiso, T. Puig, X. Obradors, *Adv. Funct. Mater.* **2009**, *13*, 2139.
[9] H. J. Fan, W. Lee, R. Hauschild, M. Alexe, G. L. Rhun, R. Scholz, A. Dadgar, K. Nielsch, H. Kalt, A. Krost, M. Zacharias, U. Gösele, *Small* **2006**, *2*, 561.
[10] S. Kodambaka, J. Tersoff, M. C. Reuter, F. M. Ross, *Science* **2007**, *316*, 729.
[11] T. Ishikawa, T. Nishimura, S. Kohmoto, K. Asakawa, *Appl. Phys. Lett.* **2000**, *76*, 167.
[12] B. Yang, F. Liu, M. G. Lagally, *Phys. Rev. Lett.* **2004**, *92*, 025502.
[13] J. H. Lee, Z. M. Wang, W. T. Black, V. P. Kunets, Y. I. Mazur, G. J. Salamo, *Adv. Funct. Mater.* **2007**, *17*, 3187.
[14] F. M. Ross, M. Kammler, M. C. Reuter, R. Hull, *Philos. Mag.* **2004**, *84*, 2687.
[15] A. Pascale, I. Berbezier, A. Ronda, P. C. Kelires, *Phys. Rev. B: Condens. Matter* **2008**, *77*.
[16] S. Kohmoto, H. Nakamura, T. Ishikawa, K. Asakawa, *Appl. Phys. Lett.* **1999**, *75*, 3488.
[17] Y. Du, J. F. Groves, I. Lyubinetsky, D. R. Baer, *J. Appl. Phys.* **2006**, *100*, 094315.
[18] M. J. Hampton, S. S. Williams, Z. Zhou, J. Nunes, D. H. Ko, J. L. Templeton, E. T. Samulski, J. M. DeSimone, *Adv. Mater.* **2008**, *20*, 2667.
[19] S. Donthu, Z. X. Pan, B. Myers, G. Shekhawat, N. G. Wu, V. Dravid, *Nano Lett.* **2005**, *5*, 1710.
[20] M. C. Wu, C. M. Chuang, Y. F. Chen, W. F. Su, *J. Mater. Chem.* **2008**, *18*, 780.
[21] X. Ma, H. Zhang, J. Xu, J. Niu, Q. Yang, J. Sha, D. Yang, *Chem. Phys. Lett.* **2002**, *363*, 579.
[22] A. G. Leyva, P. Stoliar, M. Rosenbusch, V. Lorenzo, P. Levy, C. Albonetti, M. Cavallini, F. Biscarini, H. E. Troiani, J. Curiale, R. D. Sanchez, *J. Solid State Chem.* **2004**, *177*, 3949.
[23] K. S. Shankar, A. K. Raychaudhuri, *Mater. Sci. Eng. C: Biomimetic Supramolecular Syst.* **2005**, *25*, 738.
[24] K. S. Shankar, A. K. Raychaudhuri, *Nanotechnology* **2004**, *15*, 1312.
[25] C. Li, B. Lei, Z. C. Luo, S. Han, Z. Q. Liu, D. H. Zhang, C. W. Zhou, *Adv. Mater.* **2005**, *17*, 1548.
[26] A. G. Leyva, P. Stoliar, M. Rosenbusch, P. Levy, J. Curiale, H. Troiani, R. D. Sanchez, *Physica B: Condens. Matter* **2004**, *354*, 158.
[27] P. Levy, A. G. Leyva, H. E. Troiani, R. D. Sanchez, *Appl. Phys. Lett.* **2003**, *83*, 5247.
[28] S. Dong, F. Gao, Z. Q. Wang, J. M. Liu, Z. F. Ren, *Appl. Phys. Lett.* **2007**, *90*, 082508.
[29] K. R. Bhayani, S. N. Kale, S. Arora, R. Rajagopal, H. Mamgain, R. Kaul-Ghanekar, D. C. Kundaliya, S. D. Kulkarni, R. Pasricha, S. D. Dhole, S. B. Ogale, K. M. Paknikar, *Nanotechnology* **2007**, *18*, 345101.
[30] T. Yamaguchi, S. Shimizu, T. Suzuki, Y. Fujishiro, M. Awano, *J. Electrochem. Soc.* **2008**, *11*, B1141.
[31] A. K. Pradhan, R. Bah, R. B. Konda, R. Mundle, H. Mustafa, O. Bamiduro, R. R. Rakhimov, Xiaohui Wei, D. J. Sellmyer, *J. Appl. Phys.* **2008**, *103*, 07F704.
[32] V. N. Krivoruchko, A. I. Marchenko, A. A. Prokhorov, *Low Temperature Phys.* **2007**, *33*, 433.
[33] T. Uemura, K. Sekine, K. Matsuda, M. Yamamoto, *Jpn. J. Appl. Phys.* **2005**, *44*, 2604.
[34] J.-W. Feng, L.-P. Hwang, *Appl. Phys. Lett.* **1999**, *75*, 1592.
[35] E. Ferain, R. Legras, *Nucl. Instrum. Methods Phys. Res, Section B: Beam Interactions Mater. Atoms* **2003**, *208*, 115.
[36] E. Ferain, R. Legras, *Nucl. Instrum. Methods Phys. Res, Section B: Beam Interactions Mater. Atoms* **1993**, *82*, 539.
[37] J. Bao, D. C. Bell, F. Capasso, N. Erdman, D. Wei, L. Froberg, T. Martensson, L. Samuelson, *Adv. Mater.* **2009**, *21*, 1.
[38] F. Sanchez, G. Herranz, J. Fontcuberta, M. V. Garcia-Cuenca, C. Ferrater, M. Varela, *Phys. Rev. B: Condens. Matter* **2006**, *73*, 073401.
[39] W. Van den Broek, J. Verbeeck, S. De Backer, P. Scheunders, D. Schryvers, *Ultramicroscopy* **2006**, *106*, 269.
[40] H. Zheng, Q. Zhan, F. Zavaliche, M. Sherburne, F. Straub, M. P. Cruz, L. Q. Chen, U. Dahmen, R. Ramesh, *Nano Lett.* **2006**, *6*, 1401.
[41] F. C. Frank, J. H. van der Merwe, *Proc. R. Soc. London. A: Mathematical Phys. Sci.* **1949**, *198*, 205.
[42] V. A. Shchukin, D. Bimberg, *Rev. Mod. Phys.* **1999**, *71*, 1125.
[43] J. Tersoff, F. K. Legoues, *Phys. Rev. Lett.* **1994**, *72*, 3570.
[44] J. Gutierrez, T. Puig, M. Gibert, C. Moreno, N. Roma, A. Pomar, X. Obradors, *Appl. Phys. Lett.* **2009**, *94*, 172513.
[45] T. Aytug, M. Paranthaman, J. R. Thompson, A. Goyal, N. Rutter, H. Y. Zhai, A. A. Gapud, A. O. Ijaduola, D. K. Christen, *Appl. Phys. Lett.* **2003**, *83*, 3963.
[46] Q. He, D. K. Christen, R. Feenstra, D. P. Norton, M. Paranthaman, E. D. Specht, D. F. Lee, A. Goyal, D. M. Kroeger, *Physica C.* **1999**, *314*, 105.
[47] A. Hassini, A. Pomar, J. Gutierrez, M. Coll, N. Roma, C. Moreno, A. Ruyter, T. Puig, X. Obradors, *Supercond. Sci. Technol.* **2007**, *20*, S230.
[48] The pinning force F_p is obtained from the product of $J_c(B) \cdot B$, being a true measure of the superconducting pinning performance. In particular, the critical current densities at 2 T and 77K for the standard and nanostructured films analyzed are: 3.7×10^4 A cm^{-2} and 6.6×10^4 A cm^{-2}, respectively.